4D Printing Design and Modeling in Classroom

Ali Zolfagharian[a], Hamid Reza Jarrah[b], and Mahdi Bodaghi[b]
[a]*School of Engineering, Deakin University, Geelong 3216, Australia*
[b]*Department of Engineering, School of Science and Technology, Nottingham Trent University, Nottingham NG11 8NS, United Kingdom*

Abstract

The Emergence of four-dimensional (4D) printing and bioprinting in additive manufacturing (AM), which requires knowledge of multi-physics, chemistry, and engineering skills, is bringing many engineering applications in biomedicals, wearables, and robotics. This newly emerging technology has become a feasible commercial proposition because of lower costs, more design freedom, and more rapid production methods. This serves as a significant multidisciplinary research and training platform for both academia and the professional world. This work aims at enhancing researchers' interest, knowledge, and skills in the emerging field of 4D printing and bioprinting. A greater knowledge of 4D printing and promotion of its practises enables students to pursue research and applications that 4D printing may offer. Therefore, a straightforward step-by-step approach, including design, metaphysics modeling principles, finite element method (FEM) simulation, and minimum facilities to replicate 4D bioprinting as part of an interdisciplinary unit in class, is presented in this study.

Keywords: 4D printing; bioprinting; FEM; simulation; experiment

1. Introduction

Four-dimensional (4D) bioprinting derived from three-dimensional (3D) printing in the concept of time varying characteristics of the structure after fabrication was first introduced not long ago, in 2013 [1]. Typically, smart materials, such as shape memory polymers (SMP)s [2-4] and hydrogels [5, 6], are used to offer different functionalities to 3D structures, such as shape changing, in response to a stimulus, like temperature, light, or electricity change [7]. Therefore, different aspects of the field are still being investigated in higher degree research levels through complex multi-physic modeling principles, finite element method (FEM) simulations, and experimental tests.

The 4D printing is a promising rapid and accurate manufacturing method for controlling self-morphing in custom-design structures [8-10]. This study strives to demonstrate a readily implemented practical demonstration of 4D bioprinting control parameters such as different geometrical design and stimulus effects on the bending angle of the 4D-printed structures, including physics principles, and a self-learning steps of finite element method (FEM) simulations and detailed experimental procedure.

The self-morphing 4D bioprinting refers to transformation of printed items from flat structures into 3D assemblies when an external stimulus is applied [11, 12]. Such structures have been broadly found applications in soft robotics [13, 14], packaging [15], agriculture [[16], microfluidics [17], sensors [18], metamaterials [2, 19], antenna [20], self-healing [21], and medical applications, such as minimally invasive stents [22] and drug delivery [23].

Liquid crystal gel phase transition, thermal expansion coefficient, thermal conductivity discrepancies, and differing swelling and de-swelling ratios of bi-layer or composite beams

may be used to produce spatial and temporal transformations in 4D printing [24, 25]. Direct and indirect use of active materials, such as SMPs, are producing promising results. A number of different stimuli, such electrical, magnetic, heat, light, pH, and moisture, cause these materials to deform elastically [26-28]. Extrusion-based and fused deposition modeling (FDM) 4D printing [[29] offer a straightforward approach in terms of custom pattern design and layer wise fabrication for practising the 4D printing concept compared to other methods, like stereo lithography (SLA) [30, 31], digit light processing [32], or inkjet printing [20, 33].

Light stimulus is a practical means to produce heat using a photo-thermal conversion, since it has the capacity to be remotely controlled, rapidly switches on and off, and uses clean and sustainable energy. Sunflowers are a perfect example of light-activated 4D-printed soft actuators, since they employ sunshine to perform these folding and unfolding actions [34]. Lighting from long distances allows bending without human involvement, which is of interest for a variety of applications such as the release of pharmaceuticals, the packing and the assembling of manufactured goods [35, 36]. In this case study, a simple 4D printing approach is introduced in transforming a flat sheet into spatial structure using near infrared (NIR) light. A FEM modeling of SMP substrate and 4D-printed patterns is developed. Experimental tests are carried out to validate the model. The proposed model predicts the final shape of the 4D-printed structure with excellent qualitative agreement with experimental studies. The study provides guidelines for the learning principles of 4D bioprinting, design, modeling, FEM simulation, and practical experiment of 4D bioprinting with the least equipment. This study requires the following materials:

1- An inexpensive commercial pre-strained polystyrene (PS), called Shrink Film.
2- An infrared lamp.
3- Extrudable paste, e.g., chitosan hydrogel used here.
4- Black dye, e.g., carbon black.
5- A syringe to replicate printing, e.g., Bioplotter 3D printer used here for fast and accurate manufacturing.

The PS film is used as a representative of thermo-responsive SMP as substrate material. The active hinges are made of hydrogel paste and dye in black colour and printed on PS, Shrink Film and substrate in different patterns. In response to light emission from the NIR lamp, the printed black pattern absorbs light more than the transparent PS substrate functioning as a heat source resulting in the localized heating. This causes the underlying printed area to heat up faster than the unprinted area leading to actuation due to thermal stress gradients through the thickness of the film too. Hence, the film shrinks locally at the active hinges where the temperature is exceeded the glass temperature leading to bending. The bending measures are shown to be controlled via the 3D printing features, including the geometrical properties and stimulus intensity.

The rest of paper is organised as follows. Section 2 explains the mechanism and guides through design and fabrication of the 4D-printed structure. Section 3 describes the modeling principles and details of FEM. Section 4 presents the experimental tests and discusses the results. Section 5 is the conclusion.

2. Design and Fabrication

2.1. 4D printing mechanism and design

In this work, we've chosen to print using pre-strained, or Shrink Film, since it is readily available, affordable, transparent, and has appropriate rigidity. Pre-strained Shrink Film is a PS sheet that was cooled below its glass transition temperature (T_g) while being stretched above the T_g, and then was annealed. When they are heated above T_g, these materials release their inherent tension. For this investigation, the shrinkage has been found to be up to 60% when the T_g is around $102\ °C$ [37]. When the film begins to shrink, the ratio of shrinkage accelerates and peaks about 120 °C where the shrinking ratio achieves a plateau and the curved structures restore to their flat original form. This temperature is known as softening temperature too.

A simple approach of absorbing heat is to use dark-coloured patterns that absorb NIR and function as actuator hinges. As a result, a suitable material with high light absorption and heat conversion is required to operate as a hinge to commence actuation. The non-radiative decay of light absorption in printed materials boosts the interior temperature. In other words, raising the local temperature over the glass transition temperature in the printed region of the backbone polymer causes the actuator to bend gradually.

The mismatch in temperature sensitivity between the polymer substrate and the hinge causes structural morphing. Bending of the PS film happens because of shrinkage at T_g in response to heat absorption. When heated to the glass transition temperature, the polymer chains in amorphous areas become more mobile, and the specific heat capacity rises, but the elastic modulus decreases significantly. The actuation occurs when heat is transmitted across the cross section and the T_g is attained across the gradients of the cross-section because of residual stress. However, further heating above the T_g causes an irreversible pure plastic region. Earlier studies [10] showed that different thicknesses and widths of hinges lead to sequential bending of in 4D-printed structure under even light intensity. In this study therefore, the effects of different 4D printing patterns and the number of layers for controlling the bending angle are focused while keeping the amount of printed hinge material same for a fair comparison's sake. Therefore, the same surface area with different patterns, namely square, honeycomb, and zigzag, are drawn from the centre with assumed equal extrudate thicknesses as shown in **Fig. 1.**

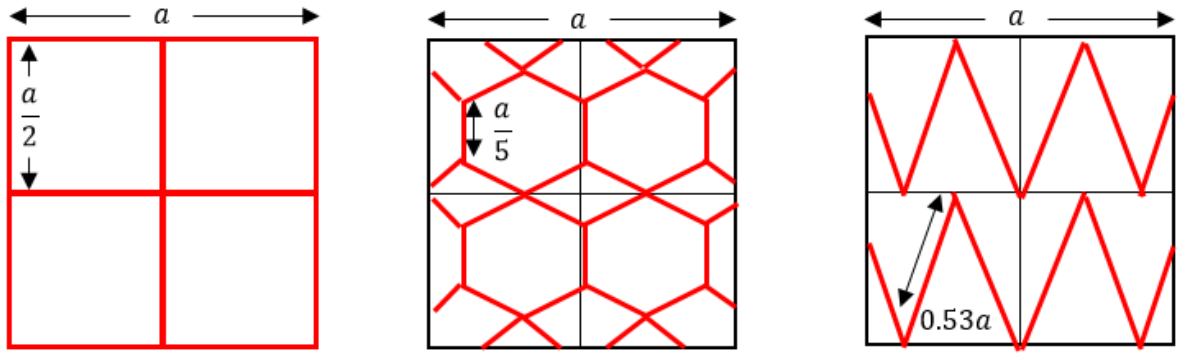

Fig. 1. Different printed active hinge patterns with same; from left to right named square, honeycomb, and zigzag, respectively.

2.2. Materials preparation and printing

First the PS films are cut into the same dimensions of $50mm \times 10mm$. Then the center of the film is marked. In general, for this experiment, any available paste that could be extruded using a syringe can be used to conduct the experiment part replicating the 4D printing. Then, the black colour paste should be prepared and loaded in a syringe and the earlier designed patterns shown in Figure 1 are 3D printed from the centre of the PS film. However, the following materials and 3D printer are employed in this study for more accurate and faster fabrication. In this work, medium molecular weight chitosan (with a deacetylation degree of 75–85%) and acetic acid were utilised (Sigma Aldrich, Australia). At 40 °C for 3 hours, a combination of 5 g chitosan in 100 ml acetic (1 *v/v* %) was formed. Following 1 hour of mixing, 250 mg of carbon black particles (Black Printer Toner Powder Laser Toner Refill for Canon with a particle size of 8–12 μm) were added to create the final polymer black. The created ink was sonicated to eliminate bubbles, since their presence degrades printing quality. The patterns illustrated in Figure 1 have a computer-aided design (CAD) model. EnvisionTEC GmbH Bioplotter was used to import the STL file (EnvisionTEC, Gladbeck, Germany). The syringe was filled with black chitosan ink [6]. As shown in **Fig. 2** and **Video S1**, several hinge designs with the same quantity of ink and strand thickness were printed in a $10mm \times 10mm$ square on the PS film. Following printing, each layer was solidified manually by pipetting a coagulant solution, including 12% (w/v) sodium hydroxide in a 7/3 water/ethanol combination, over the extruded hydrogel filaments. Then, the printed patterns are dried in an oven at 50℃ for 5 hours. This suspension was ultrasonicated for at least 1h to ensure homogeneity. Acetic acid was added to the particle suspension (2% v/v final concentration) to aid chitosan dissolution before the chitosan was dissolved with mechanical stirring for at least 3 h at room temperature (RT). The resulting paste was then centrifuged at 5752 × g for 15 min to remove bubbles.

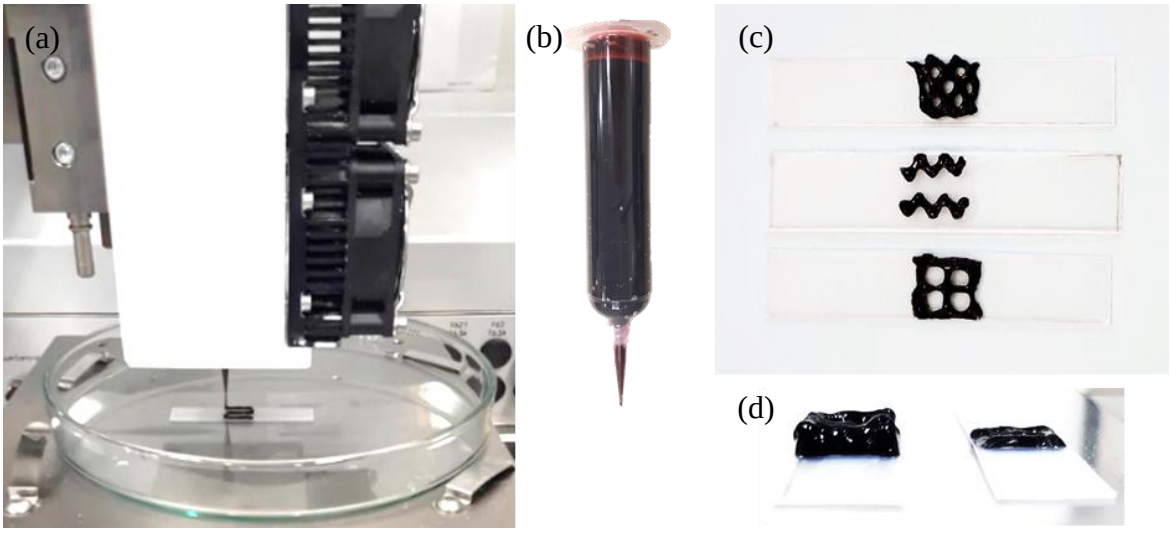

Fig. 2. (a) 3D-Bioplotter, (b) ink syringe, and (c) diverse printed hinge designs on PS film, (d) side view of the different 7 and 3-layer printed square patterns in left-right order.

2.3. Modeling of thermo-mechanical 4D-printed structure

The 4D-printed structure in this work could be investigated considering the following design parameters:

(1) The lengths, widths, and thicknesses of the printed hinge of the actuator, given by the following parameters: L, b, d, and the PS substrate length and thickness as $2S+L$ and h, respectively (**Fig. 3**).

(2) One of the 3D-printed patterns featured in the PS film's centre.

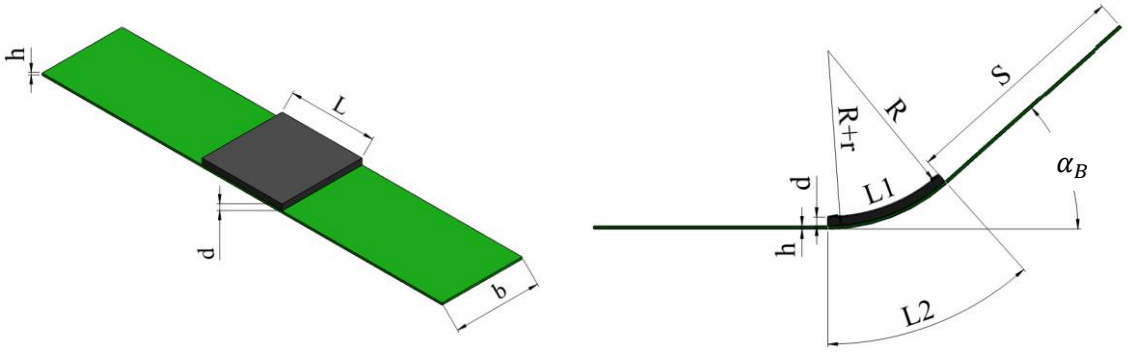

(a) (b)

Fig. 3. (a) Dimensions of the PS film and printed hinge; (b) bending parameters.

The dimensions of the printed patterns could be calculated and designed as per the parameters shown in **Fig. 1** and **Fig. 3**. In establishing the analysis of actuation, the assumption is made that the binding between the printed layer and PS film is strong enough such that the interface remains at the same length while the assembly is just being curved [31]. The bending angle will be measured in the FEM software package of ABAQUS after simulation. **Fig. 4** shows the bending angle definition in ABAQUS. Two points are chosen from PS film in the software, then with using 'Query' command the distance between these points are measured. The simple trigonometric equation, Eq.(1), calculates the angle as:

$$\tan \alpha_b = \frac{\Delta Z}{\Delta x} \tag{1}$$

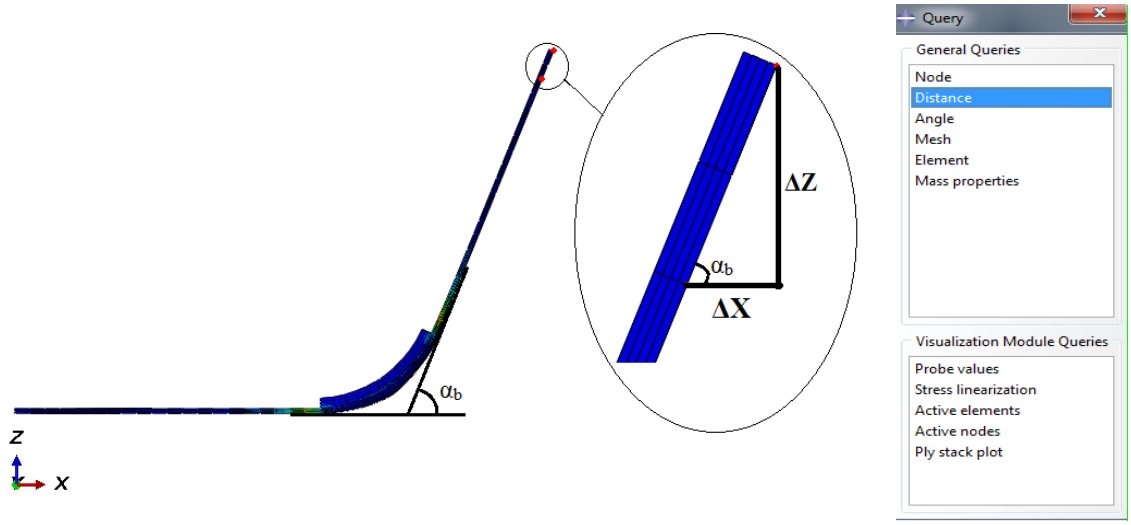

(a) (b)

Fig. 4. (a) calculation of bending angle in ABAQUS; (b) Query command.

2.4. Heat generation and temperature rise due to NIR light

It is critical to know the temperature of the actuator surface since that controls the deflection of the actuator. When the polymer film is believed to be thin enough, heating it from one side with an IR light may result in a uniform temperature increase. Assuming all heating power of IR lamp (P_{IR}) is passed on to the polymer surface, the amount of heating power (q) which is able to pass through the polymer surface with the coefficient of absorbance α that is transmitted to the polymer surface and yields an increase in temperature as:

$$q = P_{IR}\alpha = \frac{m}{A} c_p \frac{dT}{dt} \quad (2)$$

where the mass, area, temperature, and the specific heat of PS film are $m, A, T \ and \ c_p,$ respectively. Substituting the $m = \rho hA,$ where $\rho \ and \ h$ are density and thickness of film, respectively, in Eq.(2) and integrating from both sides results the total heating time (t_{IR}) required for the polymer surface temperature to reach to T_f where T_0 and T_f are initial and final temperatures of film respectively:

$$\int_0^{t_{IR}} dt = \frac{\rho h c_p}{P_{IR}\alpha} \int_{T_0}^{T_f} dT \quad (3)$$

$$t_{IR} = \frac{\rho h c_p}{P_{IR}\alpha}(T_f - T_0). \quad (4)$$

A model that shows the temperature fluctuation throughout the thickness of the PS layer over time provides further insight into actuation control. This leads to the development of a model influenced by [38]. The thermal conduction differential equation is restricted only on XY plane governed by Eq.(5) in which T is the temperature field and r', as the distance between any point and heating source on the surface, t is the time, and a is the thermal diffusivity of the film. Assuming the surface temperature is constant and ignoring the surface diffusivity as it is far lower than the thermal conduction through the Y axis (thickness direction) [9]. In small-width patterns, solving Eq.(5) results in the temperature distribution function equals to Eq.(6) where L is the printed pattern length, Q_0 is the absorbed heat from IR irradiation on surface as a single point in middle of printed pattern, and λ is the thermal conductivity of the film:

$$\frac{dT_{r'}}{dt} = a\left(\frac{\partial^2 T}{\partial x^2} + \frac{\partial^2 T}{\partial z^2}\right), \quad (5)$$

$$T_{r'} = \frac{Q_0}{4\pi\lambda L t} exp\left(-\frac{r'^2}{4at}\right) \text{ where } (r' = \sqrt{x^2 + z^2}) \quad (6)$$

The radial position of the same temperatures might be derived on basis of Eq.(6) illustrated in **Fig. 5**. The irradiation heat, $P_{IR}\alpha \times t$ could be included into the Eq.(6) as:

$$T_{r'} = \frac{P_{IR}\alpha}{4\pi\lambda L} exp(-\frac{r'^2}{4at}). \quad (7)$$

In the single point model, the maximum temperature occurs on the surface as $T_{max} = \frac{P_{IR}\alpha}{4\pi\lambda L}$. The time necessary to achieve a certain temperature for the lower surface with position ($x = 0, y = h$) may also be computed as:

$$t = \frac{-h^2}{4a \times \ln\left(\frac{4\pi\lambda L T_{r'}}{P_{IR}\alpha}\right)}. \quad (8)$$

In determining the temperature distribution of PS film over time, the following assumptions are taken into account (1) the black printed hinge pattern is a heat source comparable to the

lamp's local intensity, (2) the absorption of the light by the lines of print pattern is the sole heat source, (3) the Shrink Film's exposed surface absorbs light by 15% pattern lines of absorption (4) Initial polymer film temperatures are same with starting temperatures or ambient temperatures, and (5) the polymer film thermal conversion and heat capacity are indicated in **Table 1**. At a distance of *250 mm* from the middle point at the top of actuators, light intensity was fixed at $3.50\ mW/mm^2$. The comparison results from an increase in temperature owing to NIR irradiation from the starting temperature (*323.15 K*) are presented in **Fig. 6**. Results show that the centre point at above the actuator in the square pattern reached to the transition glass temperature of (*375.15K*) quicker than the other two. The maximum temperature should reach the film transitional glass temperature to cause bending behaviour (i.e. $T_{max} > T_g = 102$ ℃). To control the final shape accurately it is critical to control the irradiation duration in order to attain a temperature of glass above the actuator while the bottom of the actuator is more than 120 °C.

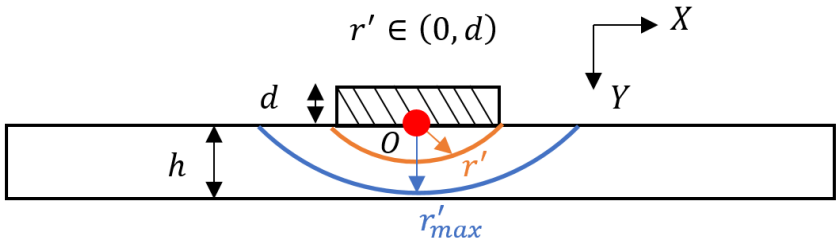

Fig. 5. The PS film surface temperature characteristics during IR irradiation.

Table 1. Specimen's physical and material properties.

Property	**Value**
Thermal conductivity ($\boldsymbol{W/mK}$)	*0.14*
NIR intensity ($\boldsymbol{mW/mm^2}$)	*3.50*
Glass temperature ($\boldsymbol{K}$)	*375.15*
Density ($\boldsymbol{kg/m^3}$)	*1050*
Distance of IR source to surface of PS ($\boldsymbol{mm}$)	*250*
Onset temperature ($\boldsymbol{K}$)	*323.15*
Thickness of PS ($\boldsymbol{mm}$)	*0.30*
Width of PS ($\boldsymbol{mm}$)	*10*
Length of PS ($\boldsymbol{mm}$)	*50*
Specific heat ($\boldsymbol{J/kgK}$)	*1300*

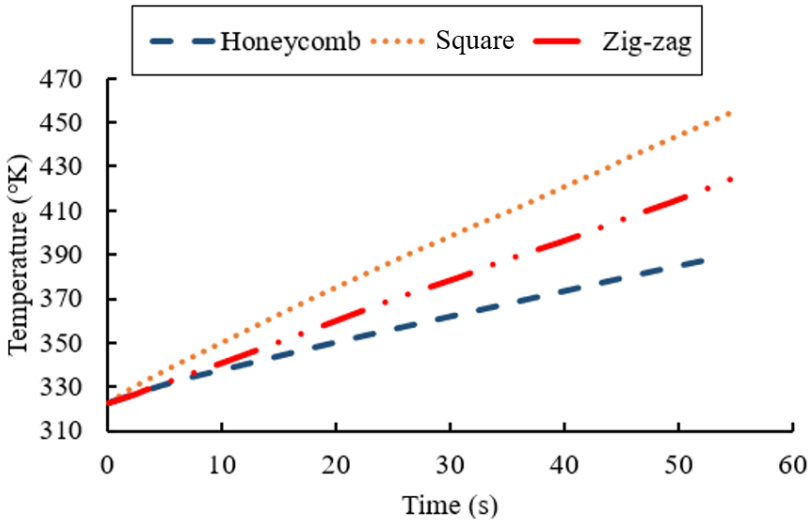

Fig. 6. Temperature on the surface of the PS film amid the actuator patterns.

2.5. FEM model of the thermal-mechanical coupling in ABAQUS

In ABAQUS, the FEM models are generated. PS film and 3D-printed design geometry are designed in CAD, then exported to ABAQUS. The default physical heat transfer model in solids is used and boundary conditions and sources are set. Based on the parameters in **Table 2** the material library is utilised and updated. Initial temperature is set at *313.15 K*, as the ambient temperature of the PS film is on the hotplate, at the time of beginning of irradiation of NIR source. A 3D model and a free tetrahedral mesh are used for the simulations.

There is a coupling between thermal and mechanical load in modeling of thermal-responsive 4D printing. For the case of thermo-elastic problems, Hook's law can be written for an isotropic material as:

$$\sigma = -\beta \Delta T \mathrm{a} + D\varepsilon \tag{9}$$

where ΔT, D, β and ε are temperature change, matrix of elastic constants, thermal stress modulus, and strain, respectively. Also, a and β are given by

$$\mathrm{a}^T = [1,1,1,0,0,0] \tag{10}$$

$$\beta = \frac{E\alpha}{(1-2\nu)} \tag{11}$$

that E, ν and α are Young's modulus, Poisson's ratio, and the thermal expansion coefficient, respectively.

The transient heat conduction equation for a 3D model in Cartesian coordinate can be written according to

$$\frac{\partial}{\partial x}\left(k_x(T)\frac{\partial T}{\partial x}\right) + \frac{\partial}{\partial y}\left(k_y(T)\frac{\partial T}{\partial y}\right) + \frac{\partial}{\partial z}\left(k_z(T)\frac{\partial T}{\partial z}\right) + G = \rho C_P \frac{\partial T}{\partial t} + \beta T \varepsilon_V \tag{12}$$

where $k_x(T)$, $k_y(T)$ and $k_z(T)$ are the temperature-dependent thermal conductivities in the x, y, and z direction, respectively. G, T, t, ρ, C_P, and ε_V, are the heat generation per unit volume, temperature, time, density, specific heat, and volume strain, respectively. Boundary and initial conditions should be considered for defining of problem. Additionally, thermoelastic deformations of interest occur during the time interval $[0, t]$.

The FEM is a numerical tool for determining approximate solutions to a large class of engineering problems. In this method, the solution region divides to non-overlapping elements. Each element is formed by the connection of a certain number of nodes. In the next step, the matrix equations that express the properties of the individual elements will be determined. These matrices involve element Left Hand Side (LHS$[k]$) matrix and load vector ($[f]$). The Global matrix for whole region should be assemble with considering LHS and load vector for each element as:

$$[K][T] = [f] \tag{13}$$

where $[T]$ is global unknown vector and

$$T(x,y,z,t) = \sum_{i=1}^{n} N_i(x,y,z)T_i(t) \tag{14}$$

In which N_i are the shape functions, n is the number of nodes in an element, and T_i shows the temperature in each node of an element. There are different methods for solving this equation and Galerkin method is chosen in this study. The Galerkin method applied to Eq.(12) could be expressed as:

$$-\int N_i\left[\frac{\partial}{\partial x}\left(k_x(T)\frac{\partial T}{\partial x}\right)+\frac{\partial}{\partial y}\left(k_y(T)\frac{\partial T}{\partial y}\right)+\frac{\partial}{\partial z}\left(k_z(T)\frac{\partial T}{\partial z}\right)+G-\rho C_P\frac{\partial T}{\partial t}-\beta T\varepsilon_V\right]d\Omega+\int N_i k_x(T)\frac{\partial T}{\partial x}l d\Gamma_q+\int N_i k_y(T)\frac{\partial T}{\partial y}m d\Gamma_q+\int N_i k_z(T)\frac{\partial T}{\partial z}n d\Gamma_q=0 \tag{15}$$

where Ω and Γ are domain of integration and boundary of domain, respectively. Also l, m, and n are the direction cosines of the appropriate outward surface normals. Additionally, the material is assumed isotropic so thermal conductivities where $k_x = k_y = k_z$. Incorporating the temperature relation in Eq.(14) into Eq.(15) yields

$$-\int_\Omega k\left[\frac{\partial N_i}{\partial x}\frac{\partial N_j}{\partial x}T_j(t)+\frac{\partial N_i}{\partial y}\frac{\partial N_j}{\partial y}T_j(t)+\frac{\partial N_i}{\partial z}\frac{\partial N_j}{\partial z}T_j(t)\right]d\Omega+\int\left[N_iG-N_i\rho C_P\frac{\partial N_j}{\partial t}T_j(t)-N_i\beta T_j(t)\varepsilon_V\right]d\Omega=0 \tag{16}$$

where i and j represent the nodes in x and y directions, respectively. The final form of Eq.(16) can be written as:

$$[C_{ij}]\left\{\frac{\partial T_j}{\partial t}\right\}+[K_{ij}]\{T_j\}=\{f_i\} \tag{17}$$

where

$$[C_{ij}]=\int \rho C_P N_i N_j d\Omega \tag{18}$$

$$[K_{ij}]=k\left[\frac{\partial N_i}{\partial x}\frac{\partial N_j}{\partial x}T_j(t)+\frac{\partial N_i}{\partial y}\frac{\partial N_j}{\partial y}T_j(t)+\frac{\partial N_i}{\partial z}\frac{\partial N_j}{\partial z}T_j(t)\right]d\Omega \tag{19}$$

$$\{f_i\}=\int N_i\left[G-\beta T_j(t)\varepsilon_V\right]d\Omega \tag{20}$$

The solution trend in the finite element software is shown in **Fig. 7** flowchart. This loop repeats as per the flowchart until the desired result is achieved.

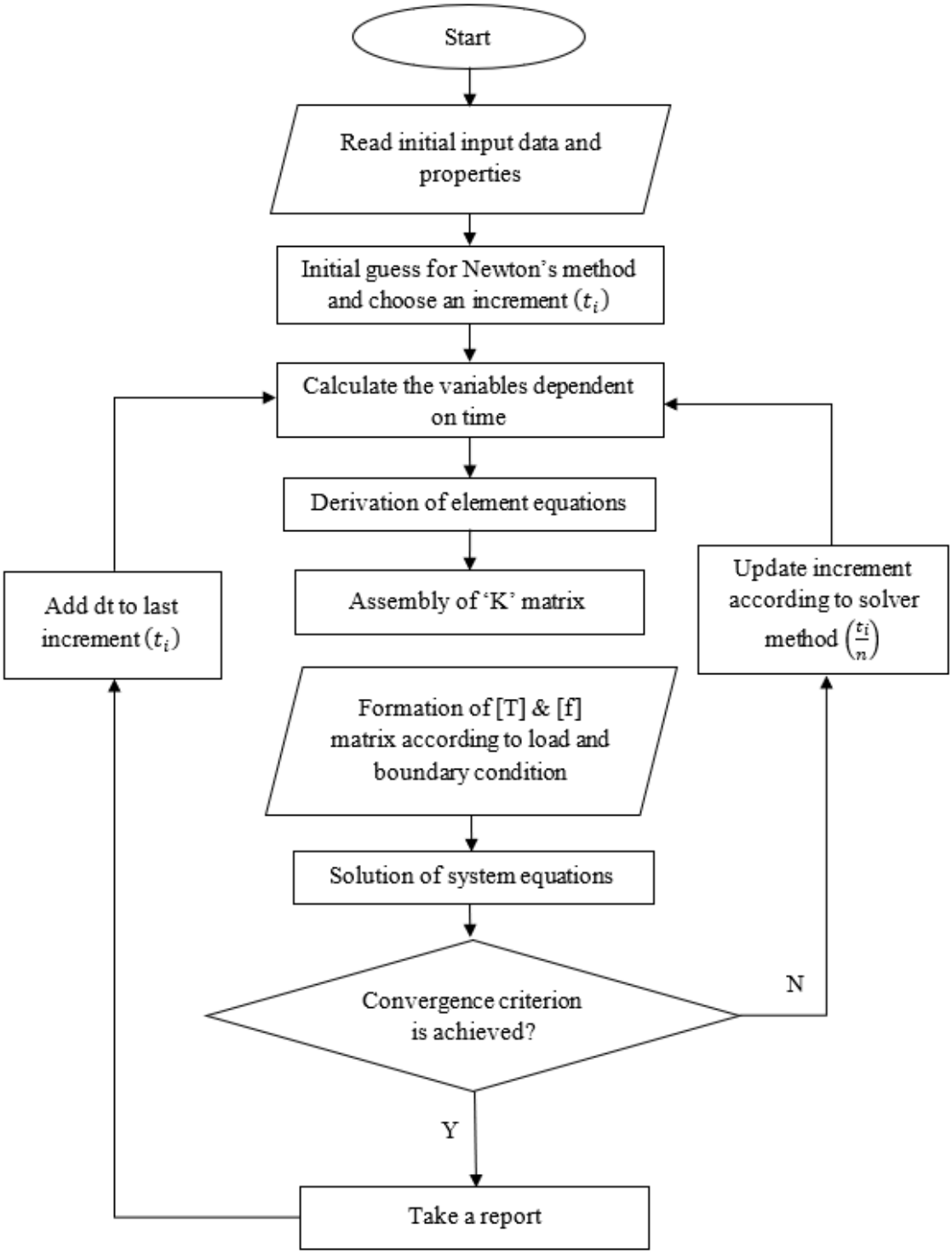

Fig. 7. Solution procedure in the FEM software

The 4D printing simulation steps with different patterns will be presented here. There are several steps, for the simulation of a model in ABAQUS software. Briefly, these steps are:

i) Create geometry of model:

First, the geometry of the model according to the dimensions of the samples will be made. In this study, the used model and elements are 3D and solid respectively. Once the model creation method is chosen, the sketch module will be opened until the sketch is drawn. This duty will be performed in the first part of the module. **Fig. 8** demonstrates the required tools for the creation of geometry.

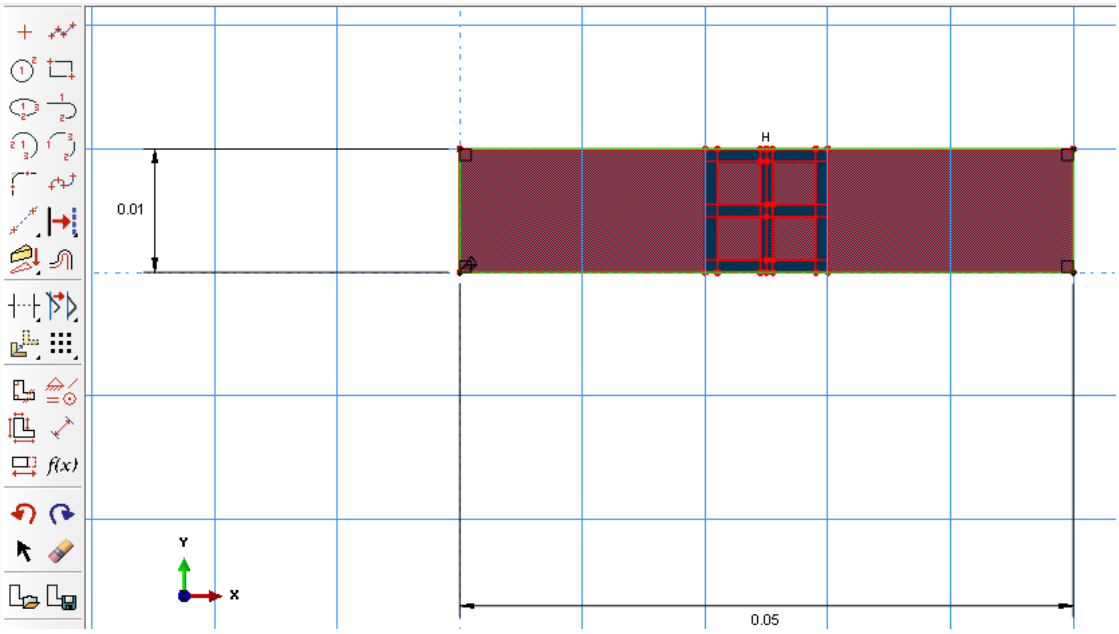

Fig. 8. The sketch environment of part module for creation of the model.

ii) Define property and assign it to the model:

This section is the main part of the simulation. The behavior of the material is known for its properties. In this study, the mechanical and thermal properties of the material should be determined. There are two materials in this study: PS film and printed hydrogel. **Table 2** shows the material properties for both adopted from [6, 39, 40].

These data will be input into the property module. Then, the specified properties will be assigned to the models. Some properties are a function of temperature. Since heating is not negligible in this model, the relation between these properties and temperature should be defined. These properties are Young's Modulus and thermal expansion coefficient. **Fig. 9** demonstrates the relation between Young's Modulus and temperature for PS film [40]. The most important of this step is to define the thermal expansion coefficient for both materials. Already, the material has a positive thermal expansion coefficient, but the film has some pre-strain. The pre-strain is reflecting the negative thermal expansion coefficient. Hence, a temperature-dependent negative thermal expansion is defined as shown in **Table 3** for both hydrogel and PS. **Fig. 10** shows the environment of this module in ABAQUS.

Table 2. Material properties of PS film and printed hydrogel.

PS			
E (Mpa)	Conductivity (w/m.°K)	Density (g/cm^3)	Specific heat (J/Kg.°K)
Fig. 9	0.14	1050	1300
Hydrogel			
E (Mpa)	Conductivity (w/m.°K)	Density (g/cm^3)	Specific heat (J/Kg.°K)
0.7	1.7	1200	1050

Table 3. Thermal expansion coefficient.

Temperature$(°K)$	273	376.5	395	410	420
Thermal expansion coefficient (α) $\left(10^{-4} \times {}^{1}/_{\circ K}\right)$	**PS**				
	0	0	-4.5	-4.5	-4.5
	Hydrogel				
	0	0	-8	-8	-8

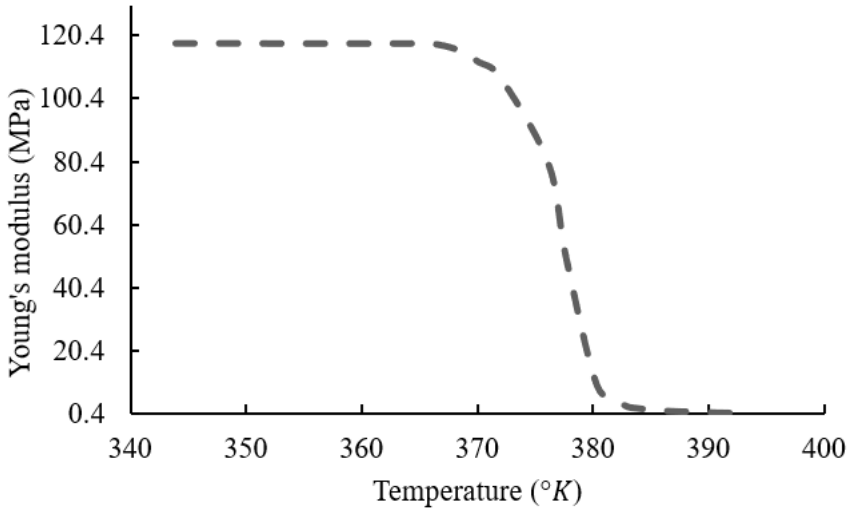

Fig. 9. Young's modulus of PS film.

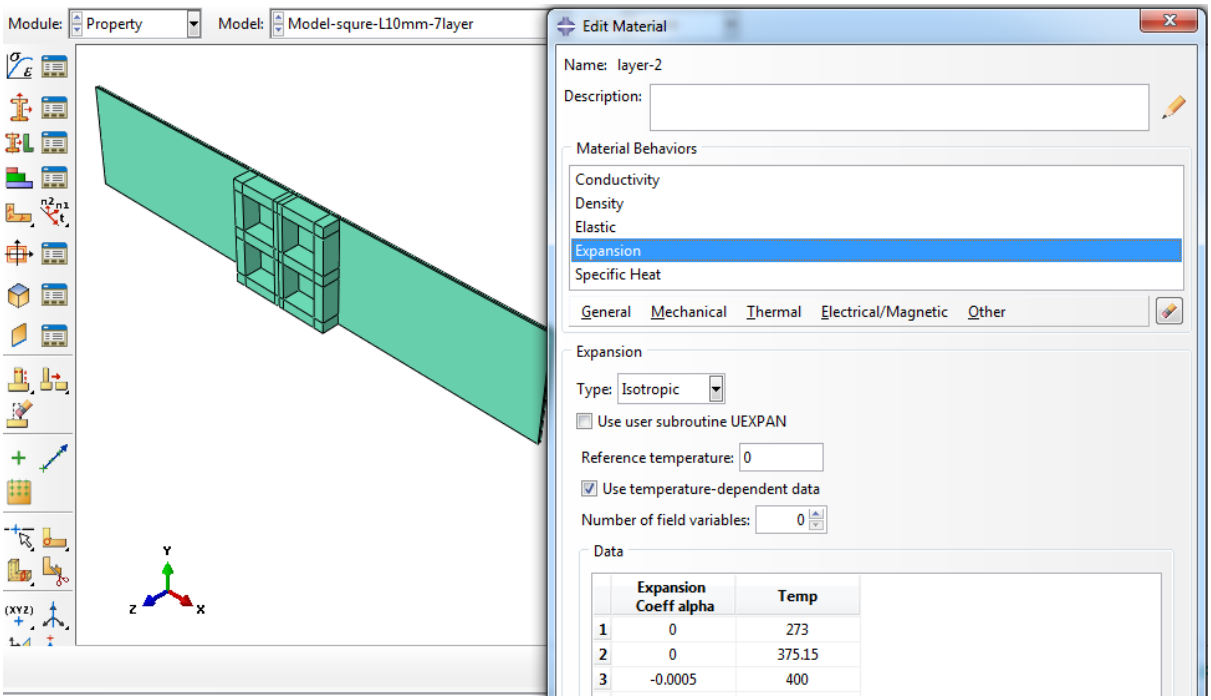

Fig. 10. The environment of property module.

iii) Define the solver

Since in this study the mechanical load is the consequence of heating, a solver coupling mechanical loading and heat transfer is required. The best solver for this problem is coupled temp-displacement. As shown in **Fig. 11**, a transient solution considering the time-dependent of temperature is chosen.

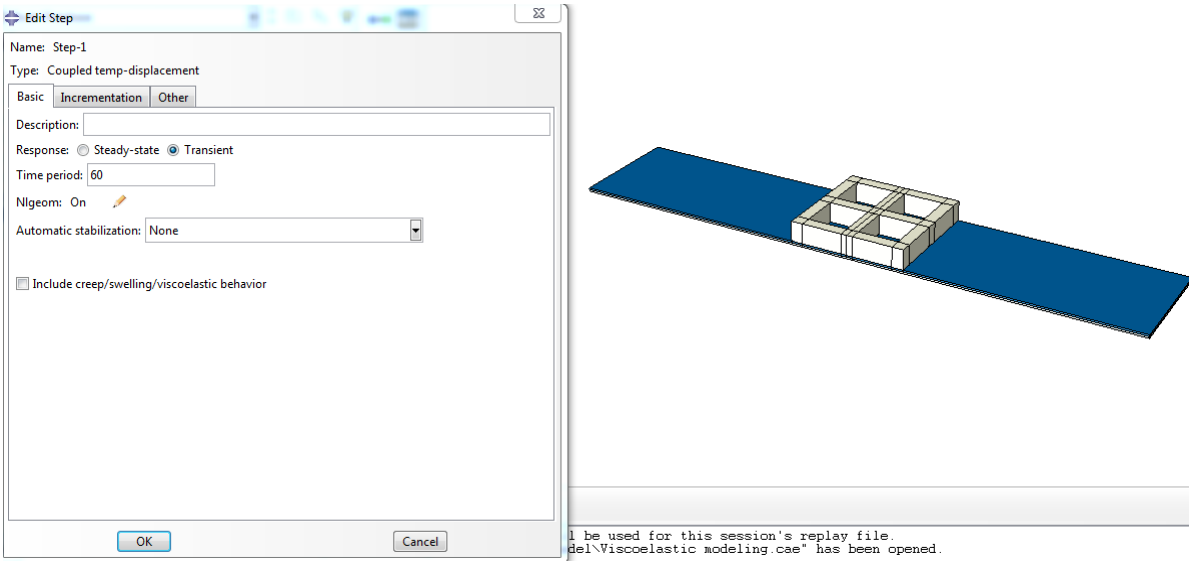

Fig. 11. Setting of the solver.

iv) Define loads and boundary conditions

Defining right boundary conditions and loads are conducted in this section. The type of loading is heat flux. The major part of heat flux will be absorbed by the hydrogel and only 15% of it will be absorbed by the film. Thus, there are two surfaces defined for applying heat: 1. Hydrogel 2. PS Film. Two types of boundary for thermal and mechanical conditions are set. For the thermal one, the initial temperature sets to 323.15 °K. For the mechanical one, the displacement in Z direction is constrained. **Fig. 12** demonstrates the applied load surface and constraints that are defined for this work.

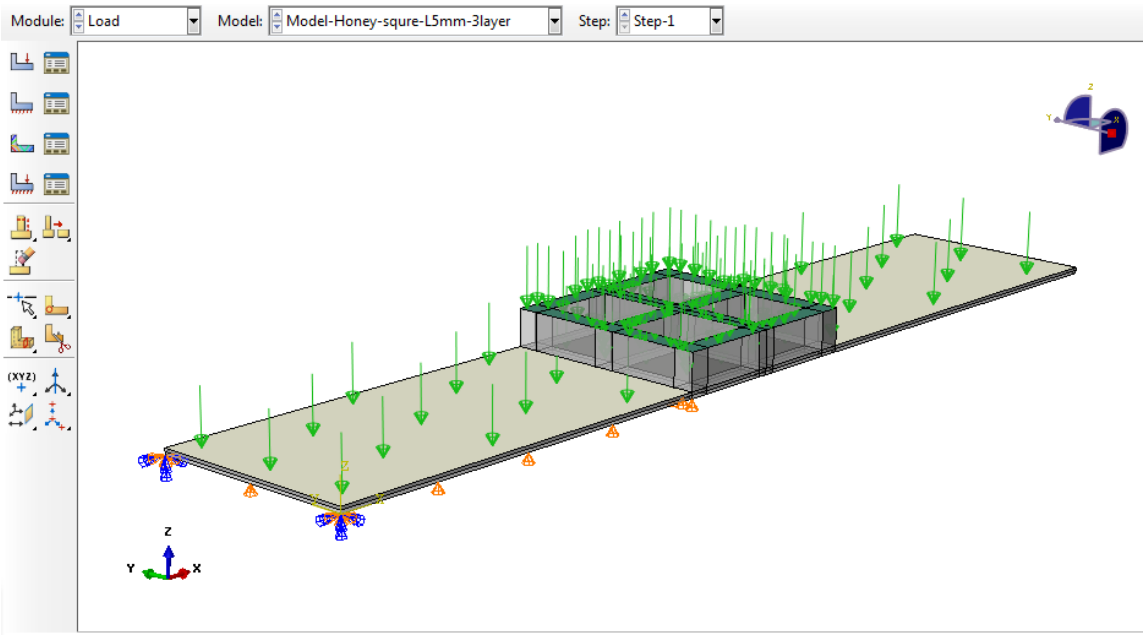

Fig. 12. Load and boundary condition module.

v) Create seeds and mesh

In this step, the size of seeds and mesh elements are specified. Indeed, the model needs mesh refinement. This is a must for the finite element method. A parameter should be considered as a criterion for mesh refinement. The bending angle is selected as a parameter for this issue. First, a large seed size is chosen for measuring the bending angle and this amount is decreased until the bending angle does not change with seed size. This procedure is conducted for each pattern with 3 layers and the results are demonstrated in **Fig. 13**. The zigzag and honeycomb patterns have acute angles, so the shape of elements in these patterns is tetrahedral, but hexahedral elements are used for the square pattern.

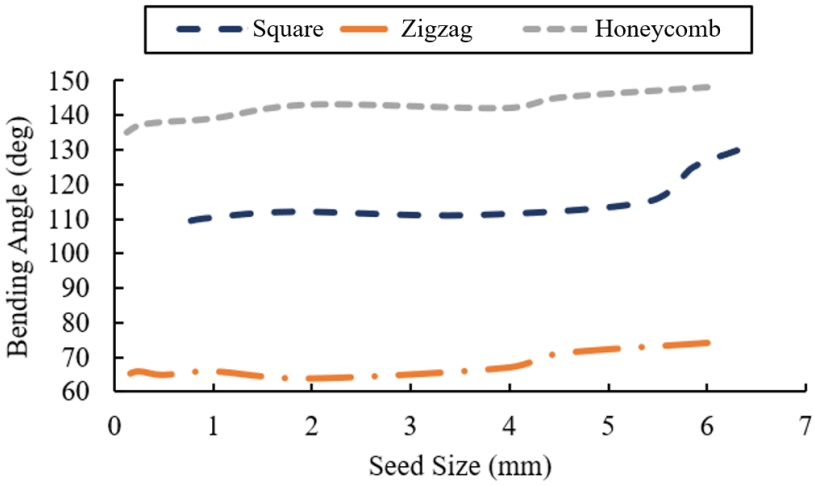

Fig. 13. Mesh refinement results.

The approximate size of seeds for the zigzag, square and honeycomb are 0.5, 0.9 and 0.5 mm respectively. Additionally, there are 3540 nodes and 2492 C3D8T elements for the creation of the mesh model as shown in **Fig. 14**. This element is an 8-node thermally coupled brick, trilinear displacement, and temperature. Also, the shape of the element is Hex-structural.

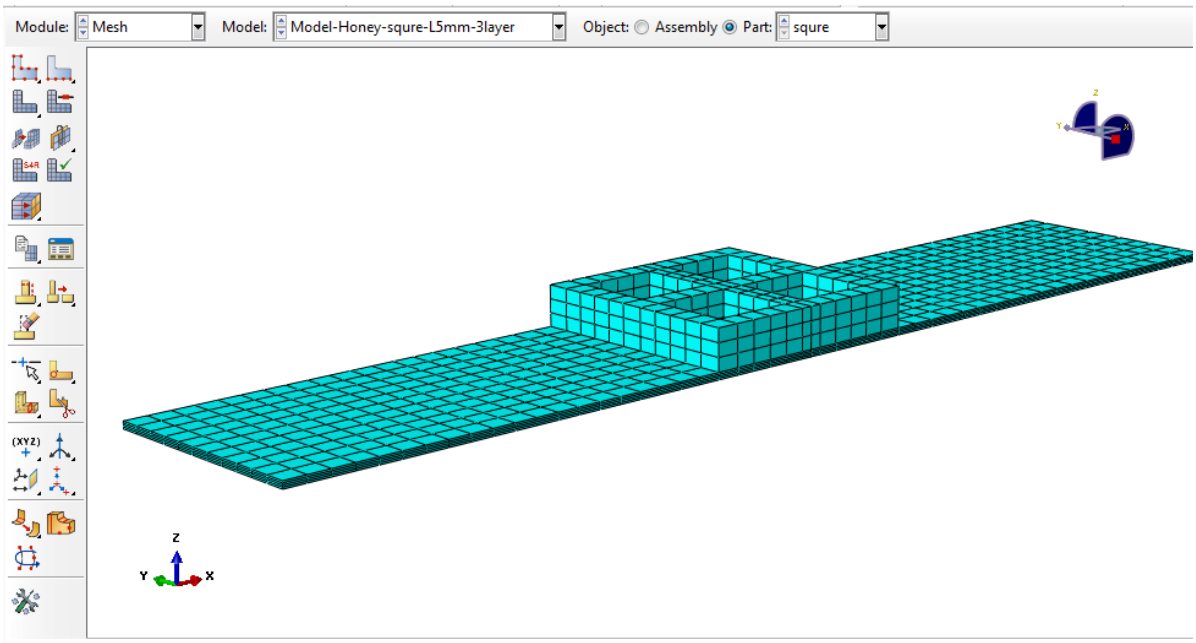

Fig. 14. The settings of mesh module.

3. Results and Discussions

A set of similar PS films (*50 mm ×10 mm*) have been prepared, using various printing parameters such as type of patterns and number of layers. The designs are printed in the centre of samples, in 3D in a *10 mm ×10 mm* area. The relation of bending angles to the 4D printing parameters is investigated by experimental tests. A hot plate provides an ambient temperature of *323.15 K*, in which the actuator is separated from the thermal plate by means of a

polydimethylsiloxane (PDMS) bar to enable an even heat all around the PS film. A NIR lamp is placed at a suitable distance (*250 mm)* to irradiate the IR light evenly on the actuator with a maximum irradiation intensity of 3.5 mW/mm^2 (**Fig. 15**). The thermographic camera shows the temperature distribution of each PS film, and a digital camera is used to capture the sample bending angles in a side view. Once the maximum deformation has been recorded before the softening temperature, the bending angle of each sample is determined. The biggest angles of bending in the honeycomb pattern is noticed when the zigzag is the smallest (see **Fig. 16** and **Fig. 17** and **Video S2**). The FEM simulation results shown in the figures are plotted at the largest bending angles achieved.

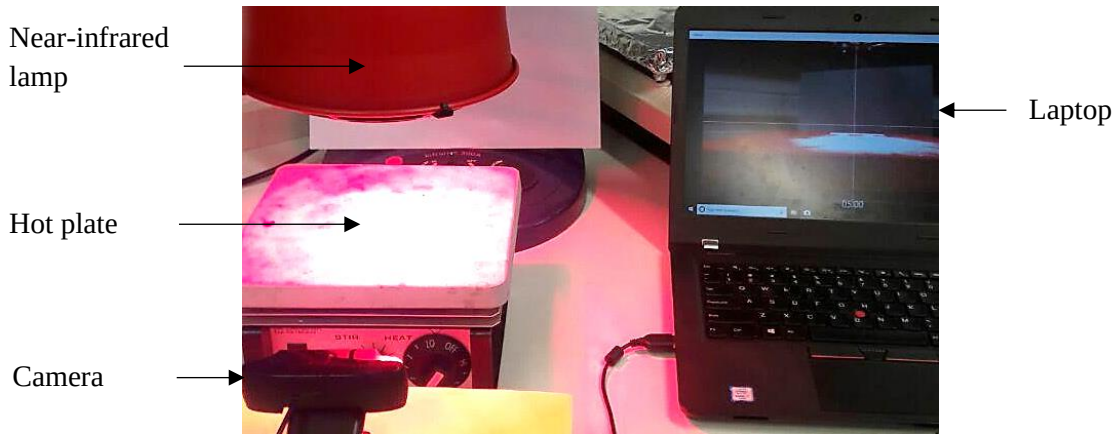

Fig. 15. Experimental set-up.

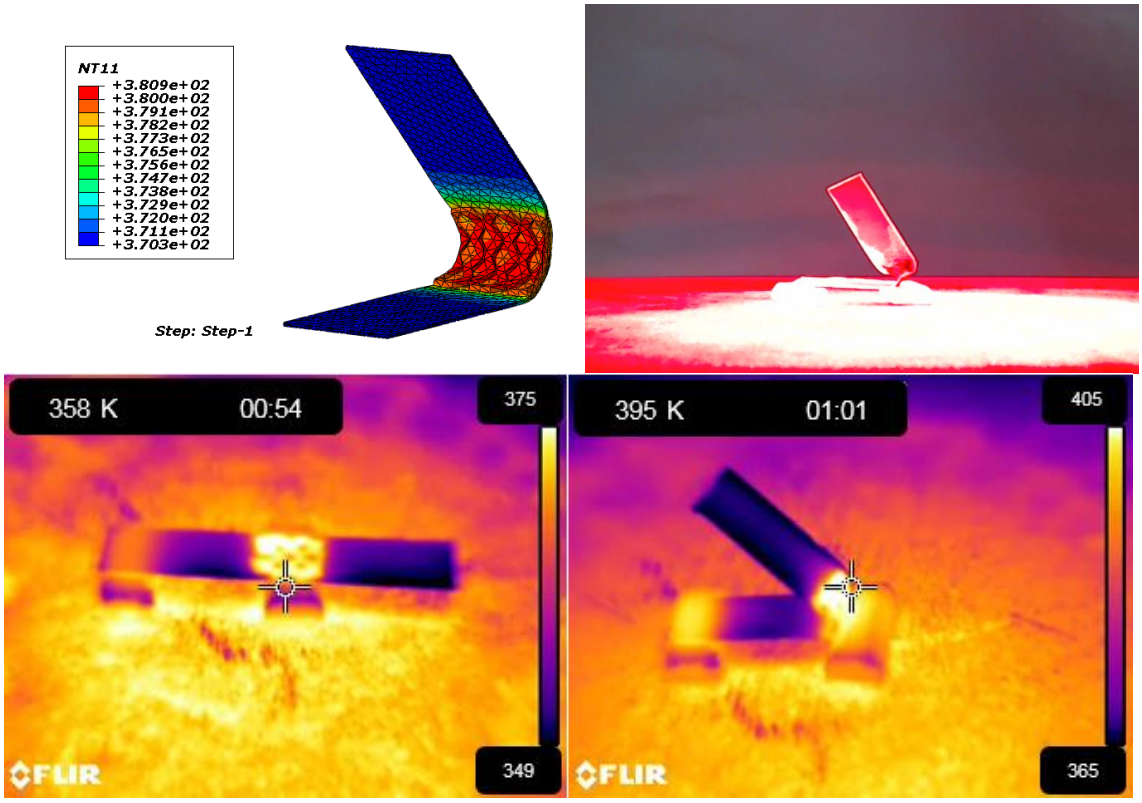

(a)

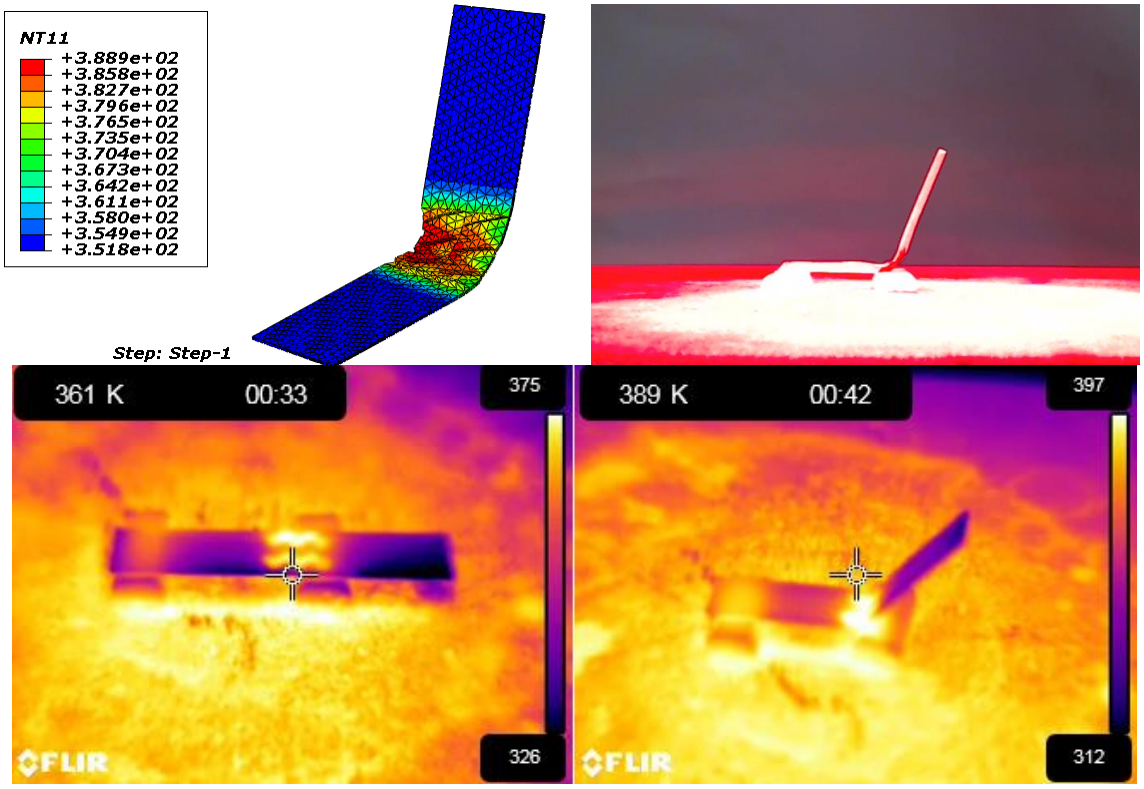

(b)

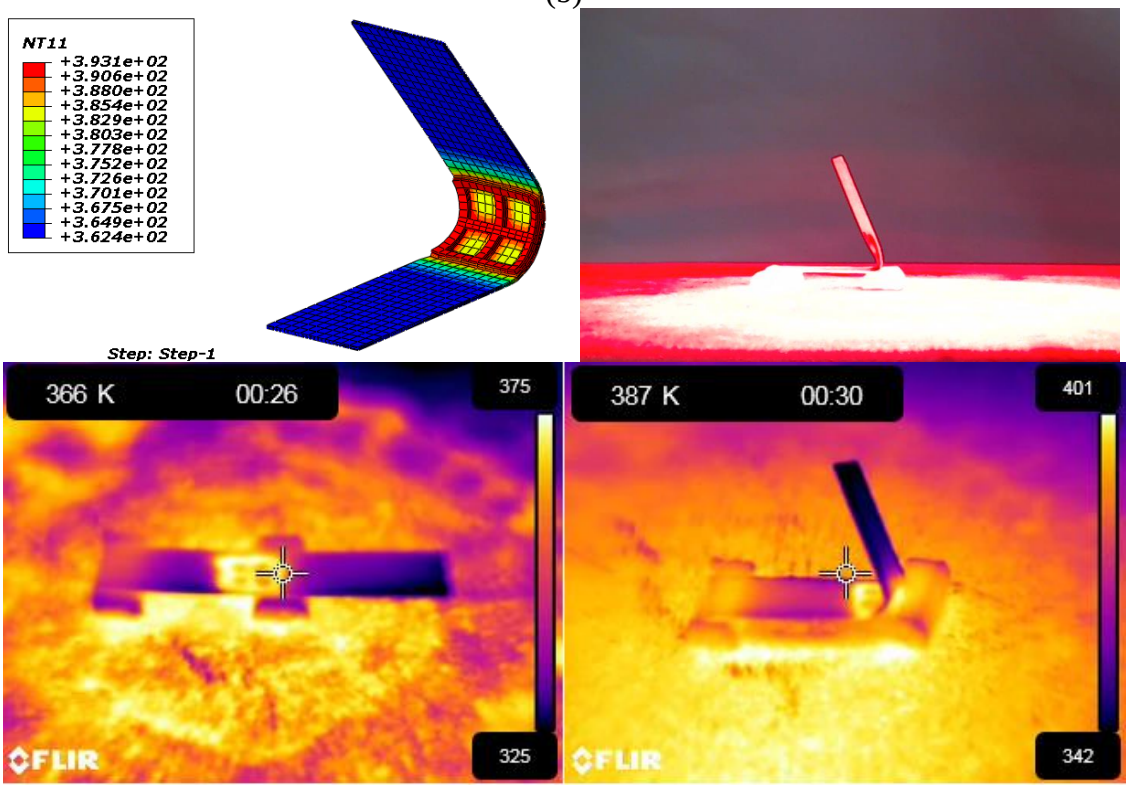

(c)

Fig. 16. Schematic comparisons of maximum bending angles resulted in FEM simulations, camera images, and thermal images for (a) honeycomb (b) zigzag (c) square patterns of 3-layer 4D-printed actuators.

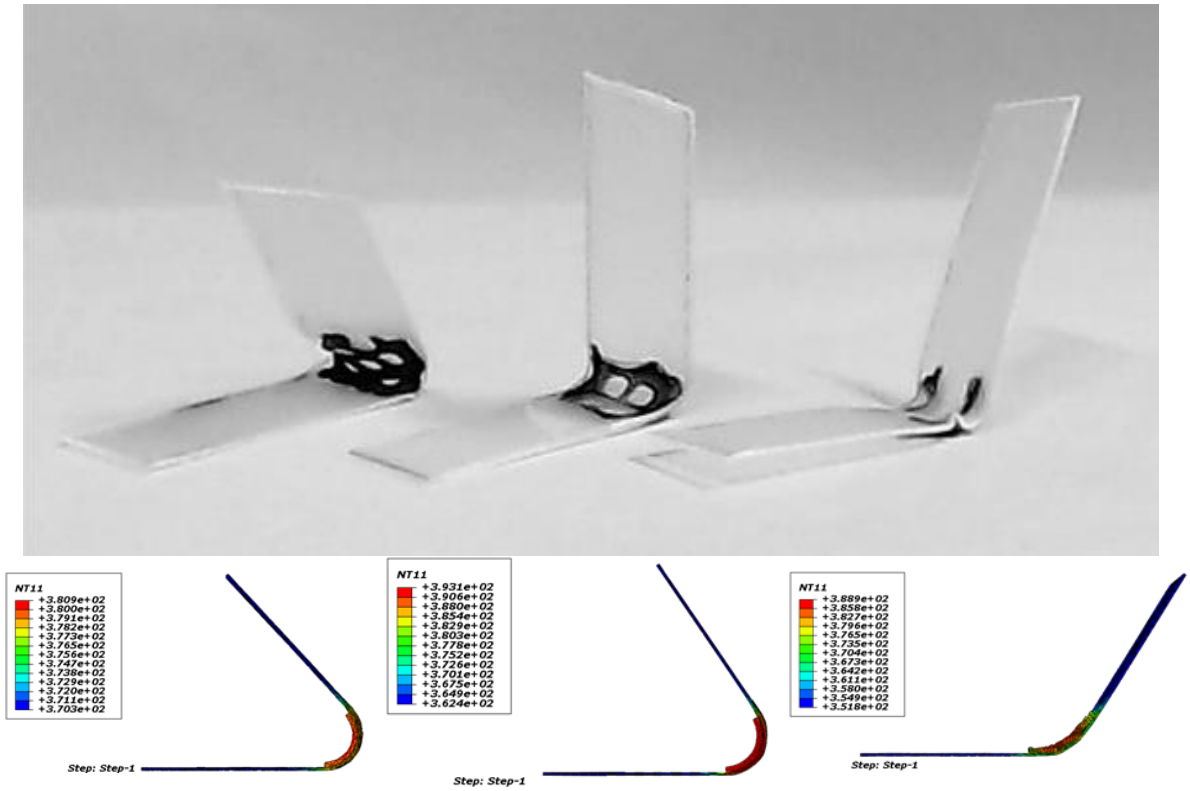

Fig. 17. Schematic comparisons of maximum bending angles resulted in FEM simulations (bottom) and experiment results (top) for honeycomb, square, and zigzag square (from left to right, respectively) patterns of 3-layer 4D printing.

The simulation and experiment are conducted for evaluating the effects of the different layers on 4D-printed structures' bending angles (**Video S3**). **Fig. 18** shows the experimental temperature rise in the middle of PS film with reasonable compatibility with FEM simulation results. **Fig. 19** compares the result of bending angle for different layers of square patterns. **Fig. 20**, also demonstrates the result of the finite element model in ABAQUS software at the last increment. Furthermore, the comparison results for other types of patterns are illustrated in **Fig. 21** and

Table 4. As seen in the

Table 4, the finite element results have appropriate compatibility with the experimental results. The errors are computed relative to the experimental results. Additionally, the error for the square pattern is less than other types of patterns. The FEM result of square type is more accurate than other patterns and the dimensions of the model are the same as reality.

Furthermore, once the thickness will be increased the error will be risen. The findings demonstrate a realistic 4D simulation model with various patterns and layer numbers. It can be noted that the maximum bending angle decreases with the number of printed layers while the actuations are delayed correspondingly. Depending on the pattern, the minimum exposure period for maximum bending is between 30 and 60 seconds. The squared pattern requires a shorter exposure period while not always resulting in the maximum bending angle. It is also noticed, however, that the largest bending angles occur during longer irradiation periods in the honeycomb pattern.

A mesh independence analysis was carried out for each of the honeycomb, zigzag and square patterns. The main reason for using tetrahedral mesh is due to the implications of various geometry-related simulations required in this study where acute angles are involved in the cross-section design of the patterns. Tetrahedral is more readily re-meshed by using a re-meshing routine in this study. Hence, using adaptive quadratic tetrahedral mesh is preferred here to other elements, such as hexahedral, to fit the arbitrary shaped geometries. The mesh refinement is also separately implemented for each pattern. Also, it was found that the simulation result was quite sensitive to the accurate value of the equivalent thermal expansion coefficient for considering pre-strain proportion of temperature.

The research successfully produced 4D-printed structures based on the same amounts of materials but varied patterns and layer control. After NIR light is exposed, the 4D-printed part begins to absorb the light and heat up, such that the pre-strained SMP underneath approaches its glass transition temperature, leading to a shrinkage in the top surface of the pre-strained film PS. In the meantime, a temperature and thus a shrinking gradient is built between the top and bottom surfaces, leading to bending the film controlled by means of 4D printing.

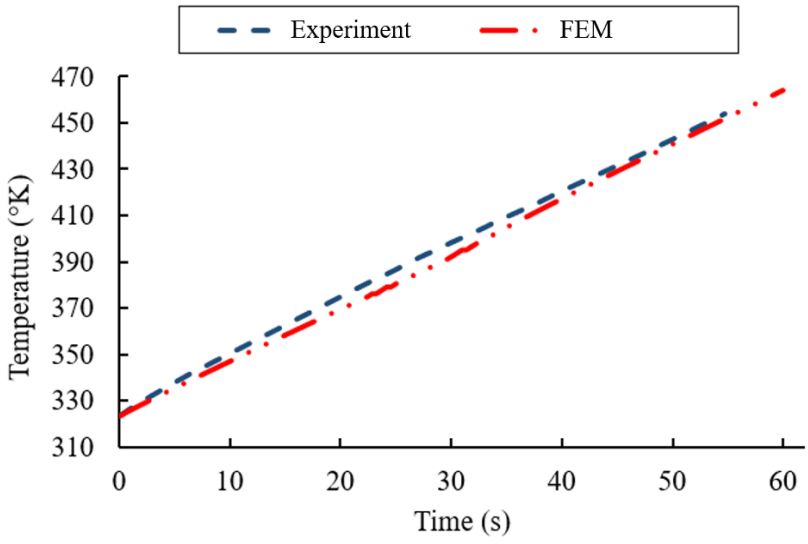

Fig. 18. Temperature in middle of printed square pattern on surface of the PS film.

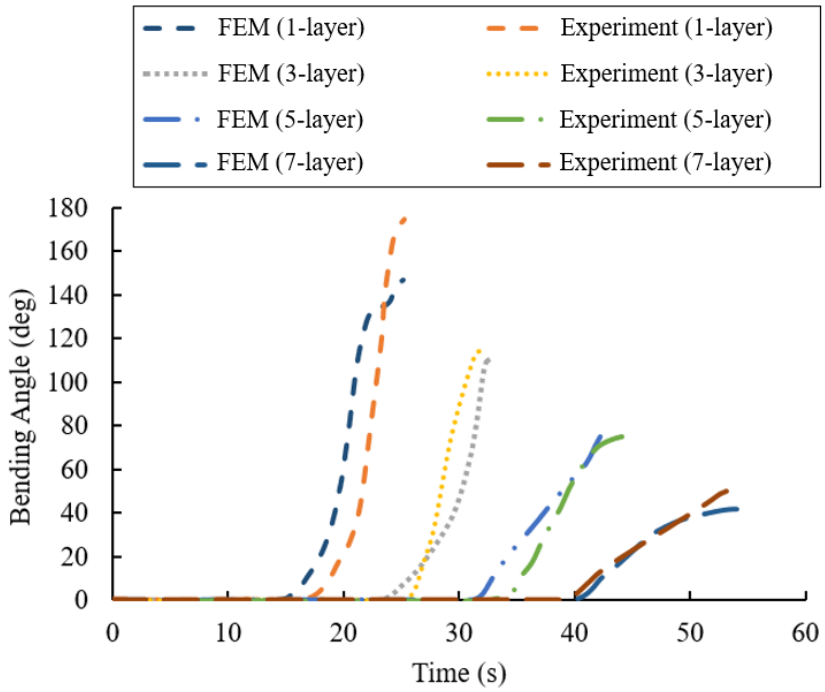

Fig. 19. Comparison results of bending angles for square pattern with different layers.

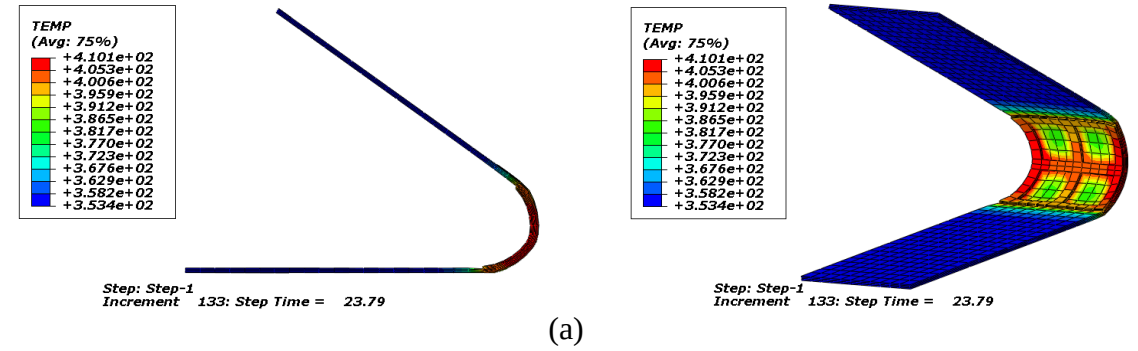

(a)

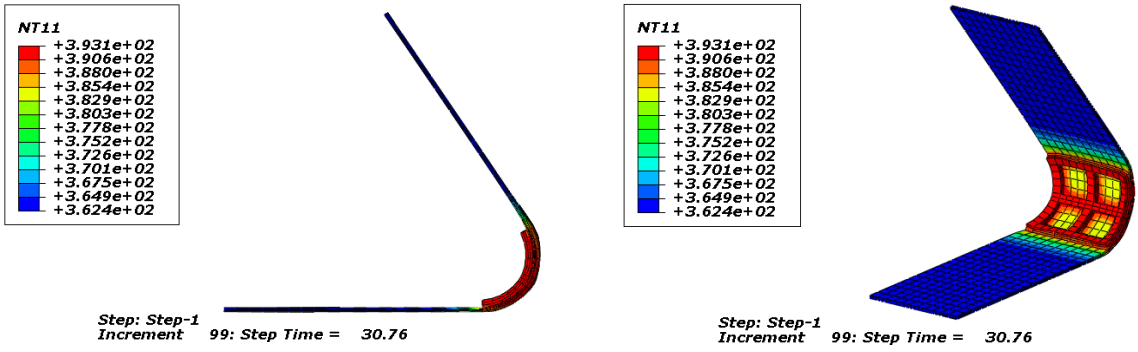

(b)

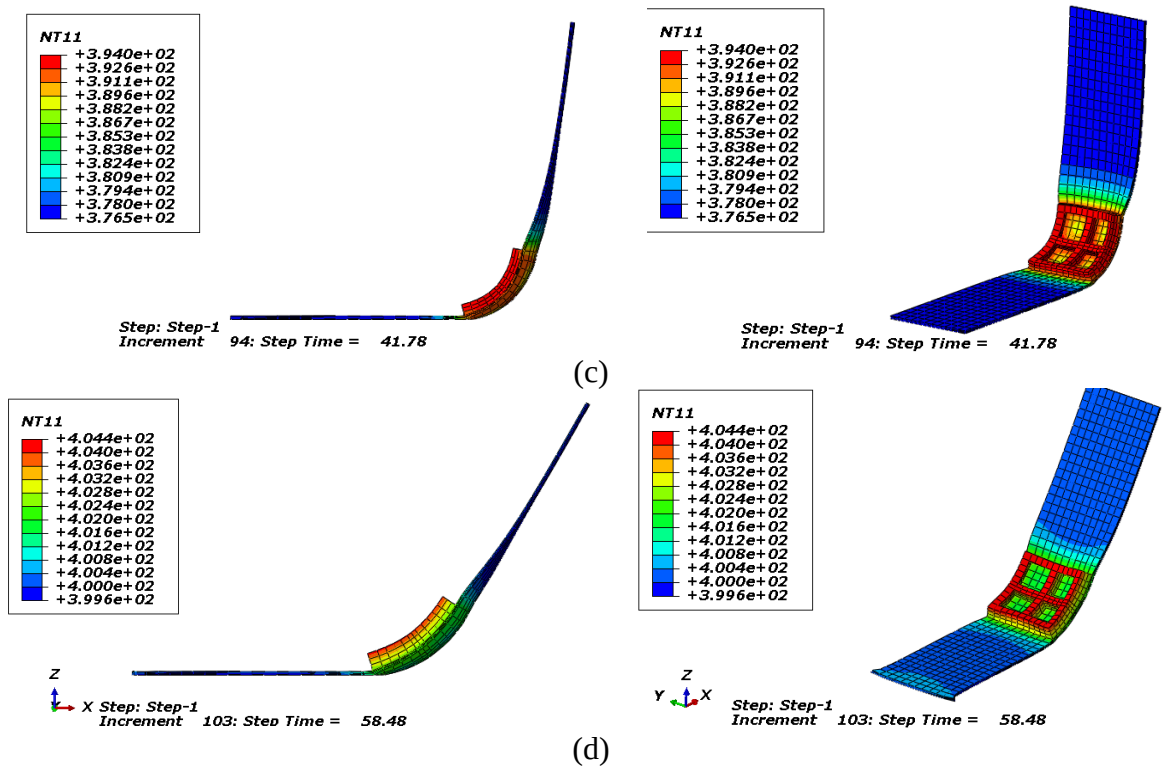

Fig. 20. Illustrations of finite element results for different layers. (a) 1-layer (b) 3-layer (c) 5-layer (d) 7-layer.

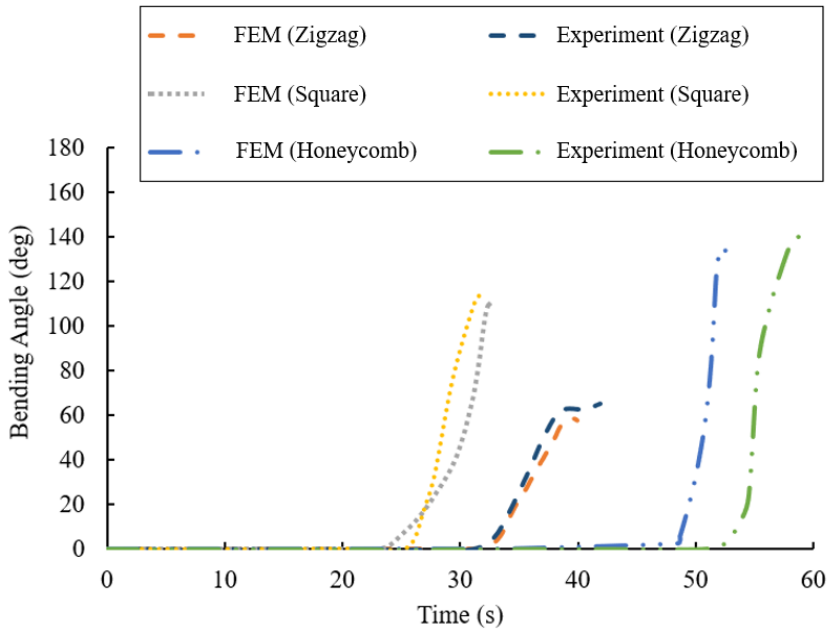

Fig. 21. Comparison results of bending angles for different patterns with 3-layer.

Table 4. Parameters of verification test results.

Printed pattern	*No. of layers*	*L (mm)*	*Bending angle (°)*				
			Estimated	**Experimental**	**FEM**	**Error % (Exp)**	**Error % (FEM)**
Honeycomb	1	2.5	139	147	141	5.44	4.08
	3	5	128	120	115	6.67	4.16
	5	7.5	71	67	70	5.97	4.47
	7	10	57	62	67	8.06	8.06
Zigzag	1	2.5	88	95	91	7.37	4.21
	3	5	79	72	75	9.72	4.16
	5	7.5	41	45	48	8.89	6.66
	7	10	33	30	33	10.00	10
Square	1	2.5	113	106	104	6.60	1.88
	3	5	98	91	88	7.69	3.29
	5	7.5	49	53	56	7.55	5.66
	7	10	39	36	38	8.33	5.55

4. Conclusions

The increased usage of additive manufacturing technology and smart materials in the industry means that companies are seeking to develop and manage production systems for academics with multidisciplinary abilities and knowledge. This paper proposed an easy to implement and follow 4D bioprinting module well designed for students and early career researchers to the field to learn different aspects of skills and knowledge as part of their engineering course giving them a valuable advantage in an increasingly competitive job market and higher degree research.

In this study, controlled bending of structures using 4D printing was presented. To fulfil the main aim of the work to be reproducible for engineering students and lecturers to practice 4D printing in class, the minimum requirements of facilities and materials to replicate the 4D printing were opted. A commercial thermoplastic PS Shrink SMP Film, a black colour paste, syringe to replicate 4D printing, a NIR lamp, are required to print spatial patterns on the SMP substrates. In order to produce asymmetric shrinkage across the thickness of the SMP hinge, a photo-thermal stimulation was applied. It was tested in an experimental context and by means of a Finite Element Model (FEM) to observe and describe the thermal response of the printed actuator hinge to NIR irradiation. To estimate the bending behaviour of the 4D-printed structure, a thermal-structural FEM model was developed in ABAQUS. The testing results confirmed the validity of the model and demonstrated that the model used in controlling the 4D printing bending angles was successful. By adjusting the 3D printing parameters, such as the pattern type and the number of layers, it was proved that the bending angle could be controlled. The present study could be utilized in different inter-disciplinary engineering courses and classes to teach and practice 4D printing via both theoretical modeling and the practical experiments.

Funding

We thank Faculty of Science, Engineering and Built Environment, Deakin University, for 2021 Mini ARC Analog Program (MAAP)—Discovery 253101, for financial support.

Declaration of competing interest

The authors declare that they have no known competing financial interests or personal relationships that could have appeared to influence the work reported in this paper.

References

1. Tibbits, S., *4D printing: multi-material shape change.* Architectural Design, 2014. **84**(1): p. 116-121.
2. Bodaghi, M., et al., *Reversible energy absorbing meta-sandwiches by FDM 4D printing.* International Journal of Mechanical Sciences, 2020. **173**: p. 105451.
3. Bodaghi, M., A. Damanpack, and W. Liao, *Adaptive metamaterials by functionally graded 4D printing.* Materials & Design, 2017. **135**: p. 26-36.
4. Bodaghi, M., A. Damanpack, and W. Liao, *Self-expanding/shrinking structures by 4D printing.* Smart Materials and Structures, 2016. **25**(10): p. 105034.
5. Zolfagharian, A., et al. *3D printed hydrogel soft actuators*. in *2016 IEEE Region 10 Conference (TENCON)*. 2016. IEEE.
6. Zolfagharian, A., et al., *Topology-optimized 4D printing of a soft actuator.* Acta Mechanica Solida Sinica, 2019: p. 1-13.
7. Zolfagharian, A., et al., *Evolution of 3D printed soft actuators.* Sensors and Actuators A: Physical, 2016. **250**: p. 258-272.
8. Bodaghi, M., et al., *4D printing self-morphing structures.* Materials, 2019. **12**(8): p. 1353.
9. Zolfagharian, A., et al., *Pattern-driven 4D printing.* Sensors and Actuators A: Physical, 2018. **274**: p. 231-243.
10. Zolfagharian, A., et al., *3D Printing of a Photo-thermal Self-folding Actuator.* KnE Engineering, 2017. **2**(2): p. 15-22.
11. Arazoe, H., et al., *An autonomous actuator driven by fluctuations in ambient humidity.* Nature materials, 2016. **15**(10): p. 1084-1089.
12. Liu, C., et al., *Remotely Controlled Microscale 3D Self-Assembly Using Microwave Energy.* Advanced Materials Technologies, 2017.
13. Onal, C.D., et al., *Origami-inspired printed robots.* IEEE/ASME Transactions on Mechatronics, 2015. **20**(5): p. 2214-2221.
14. Han, Y.L., et al., *Liquid on Paper: Rapid Prototyping of Soft Functional Components for Paper Electronics.* Scientific reports, 2015. **5**.
15. Peraza-Hernandez, E.A., et al., *Origami-inspired active structures: a synthesis and review.* Smart Materials and Structures, 2014. **23**(9): p. 094001.
16. Shin, B., et al. *Self-assembling sensors for printable machines*. in *2014 IEEE International Conference on Robotics and Automation (ICRA)*. 2014. IEEE.
17. Saez, J., et al., *On-demand generation and removal of alginate biocompatible microvalves for flow control in microfluidics.* Sensors and Actuators B: Chemical, 2016. **234**: p. 1-7.
18. Khosravani, M.R. and T. Reinicke, *3D-printed sensors: Current progress and future challenges.* Sensors and Actuators A: Physical, 2020. **305**: p. 111916.
19. Khosravani, M.R. and T. Reinicke, *Experimental characterization of 3D-printed sound absorber.* European Journal of Mechanics-A/Solids, 2021. **89**: p. 104304.
20. Kimionis, J., et al., *3D-Printed Origami Packaging With Inkjet-Printed Antennas for RF Harvesting Sensors.* IEEE Transactions on Microwave Theory and Techniques, 2015. **63**(12): p. 4521-4532.
21. Habault, D., H. Zhang, and Y. Zhao, *Light-triggered self-healing and shape-memory polymers.* Chemical Society Reviews, 2013. **42**(17): p. 7244-7256.
22. Gultepe, E., et al., *Biopsy with Thermally-Responsive Untethered Microtools.* Advanced materials, 2013. **25**(4): p. 514-519.
23. Li, M., et al., *Capillary Origami Inspired Fabrication of Complex 3D Hydrogel Constructs.* Small, 2016.

24. Kamal, T. and S.-y. Park, *Shape-Responsive Actuator from a Single Layer of a Liquid-Crystal Polymer.* ACS applied materials & interfaces, 2014. **6**(20): p. 18048-18054.
25. Zeng, H., et al., *Self-Regulating Iris Based on Light-Actuated Liquid Crystal Elastomer.* Advanced Materials, 2017.
26. Tolley, M.T., et al., *Self-folding origami: shape memory composites activated by uniform heating.* Smart Materials and Structures, 2014. **23**(9): p. 094006.
27. de Haan, L.T., et al., *Accordion-like Actuators of Multiple 3D Patterned Liquid Crystal Polymer Films.* Advanced Functional Materials, 2014. **24**(9): p. 1251-1258.
28. Zarek, M., et al., *3D Printing of Shape Memory Polymers for Flexible Electronic Devices.* Adv Mater, 2015.
29. Yang, H., et al., *3D Printed Photoresponsive Devices Based on Shape Memory Composites.* Advanced Materials, 2017.
30. Choong, Y.Y.C., et al., *4D printing of high performance shape memory polymer using stereolithography.* Materials & Design, 2017. **126**: p. 219-225.
31. Deng, D. and Y. Chen, *Origami-based self-folding structure design and fabrication using projection based stereolithography.* Journal of Mechanical Design, 2015. **137**(2): p. 021701.
32. Zhao, Z., et al., *Desolvation induced origami of photocurable polymers by digit light processing.* Macromolecular rapid communications, 2016.
33. Hubbard, A.M., et al., *Controllable curvature from planar polymer sheets in response to light.* Soft Matter, 2017. **13**(12): p. 2299-2308.
34. Atamian, H.S., et al., *Circadian regulation of sunflower heliotropism, floral orientation, and pollinator visits.* Science, 2016. **353**(6299): p. 587-590.
35. Sumaru, K., et al., *Photoresponsive polymers for control of cell bioassay systems.* Polymeric biomaterials, 3rd edn. CRC Press, Boca Raton, 2013: p. 683-708.
36. Nakata, K., et al., *Bending motion of a polyacrylamide/graphite fiber driven by a wide range of light from UV to NIR.* Materials Letters, 2012. **74**: p. 68-70.
37. Liu, Y., et al., *Self-folding of polymer sheets using local light absorption.* Soft Matter, 2012. **8**(6): p. 1764-1769.
38. Deng, D., et al., *Accurately controlled sequential self-folding structures by polystyrene film.* Smart Materials and Structures, 2017. **26**(8).
39. Werner, J. and M. Buse, *Temperature profiles with respect to inhomogeneity and geometry of the human body.* Journal of Applied Physiology, 1988. **65**(3): p. 1110-1118.
40. Mailen, R.W., et al., *A fully coupled thermo-viscoelastic finite element model for self-folding shape memory polymer sheets.* Journal of Polymer Science Part B: Polymer Physics, 2017. **55**(16): p. 1207-1219.